Dalton Transactions

ROYAL SOCIETY OF CHEMISTRY

PAPER

View Article Online
View Journal | View Issue

Cite this: *Dalton Trans.*, 2026, **55**, 3709

NIR-responsive upconversion nanoplatforms: an anionic drug carrier for ROS amplification induced by β-amyloid fibrils

Xiaofeng Jia, Yijia Guan, * Weijie Cao, Xiaoshuo Zhang, Huazhen Duan, Hui Guo, Huichang Chen, Binbin Wang, Tao Li * and Jianguo Liao

Alzheimer's disease (AD), marked by the misfolding/aggregation of β-amyloid (Aβ), is a major global health challenge. Polyoxometalates (POMs), as anionic therapeutic agents, exhibit potential in depolymerizing Aβ fibrils, inhibiting Aβ fibrillation, and acting as a photocatalyst. To achieve targeted reactive oxygen species (ROS) amplification, we developed a chitosan-modified near-infrared (NIR)-responsive upconversion nanoplatform, UCNPs(Tm/Er)@SiO_2@GPS@CH, as a targeted carrier for POMs. The nanoplatform was constructed by sequentially modifying upconversion nanoparticles (UCNPs) with a silica layer, 3-glycidoxypropyltrimethoxysilane (GPS, as a linker), and chitosan (CH, a cationic biomacromolecule). The cationic CH layer enabled efficient loading of anionic POMs through electrostatic interactions with an optimal POM loading capacity of 415.41 μg mg^{-1} that positively correlated with CH modification levels. Under NIR irradiation, the nanoplatform triggered a photodynamic effect with abundant ROS. Notably, compared with the control group and Aβ monomer group, the ROS generation in the Aβ fibril group was approximately doubled, which further enhanced the targeted therapeutic efficacy of the system. By integrating NIR responsiveness, cationic chitosan, targeted ROS generation, and low systemic toxicity, the nanoplatform provides a novel strategy for the photooxidative treatment of AD and offers insights into the design of chitosan-modified upconversion nanoparticle-based drug carrier systems.

Received 31st December 2025,
Accepted 4th February 2026

DOI: 10.1039/d5dt03121d

rsc.li/dalton

1. Introduction

As the most prevalent cause of dementia, Alzheimer's disease (AD) is estimated to account for 60% to 80% of such cases.[1,2] AD, a neurodegenerative disorder associated with cognitive impairment, is pathologically defined by the accumulation of two hallmark lesions: extracellular β-amyloid (Aβ)-containing plaques and intracellular tau-containing neurofibrillary tangles.[3,4] There is no established way to prevent AD, and currently, no cure exists for this neurodegenerative disorder.[5] Due to the large number of people worldwide suffering from AD and the devastating effects of dementia on individuals, families, communities, and healthcare systems, finding approaches to prevent, slow progression of, better manage, and cure AD is a top priority for global research centers.[6–8] At present, a growing number of studies indicate that the toxicity of Aβ monomers and fibrils was significantly reduced after specific photooxidation reactions.[9–12] Therefore, a promising research hotspot in AD therapy involves modifying the chemical structure of Aβ. This can be achieved by regulating the oxidation reaction of Aβ through photodynamic therapy (PDT), thereby inhibiting Aβ aggregation and promoting its degradation.[13–15]

Photodynamic therapy (PDT) is an emerging therapeutic approach that enables effective local control of targeted conditions. It can be applied to kill tumor cells and bacteria by activating photosensitizers with specific wavelengths to produce cytotoxic substances, namely reactive oxygen species (ROS).[16] Although PDT was mainly aimed at tumor treatment at first,[17] with the deepening of research, PDT showed great potential in photooxidation inhibition and depolymerization of Aβ.[18] Specifically, the mechanism of catalytic oxidation of Aβ by PDT can be described as the oxidation of amino acids (methionine, tyrosine and histidine) on the Aβ peptide chain by ROS produced *via* PDT, which increases the hydrophilicity of the Aβ surface and reduces the aggregation of Aβ.[12,13] One of the first conditions for the application of PDT in the treatment of brain diseases is that the light source can pass through the skull to reach the treatment site. Among many light sources used in PDT, near infrared (NIR) light falls within the biological window of the infrared spectrum (700–1700 nm). It exhibits excellent tissue penetrability and

School of Materials Science and Engineering, Henan Polytechnic University, Jiaozuo, 454003, China. E-mail: guanyj@hpu.edu.cn, taoli17@hpu.edu.cn

minimal damage to human tissues, enabling it to penetrate extracranial tissues and reach the human brain.[9,19,20] Therefore, the PDT drug system with NIR as the excitation light source has been widely used in the treatment of AD.

Lanthanide (Ln^{3+})-doped upconversion nanoparticles (UCNPs) are capable of absorbing several low-energy photons (NIR light) and emitting photons with higher energy (UV/Vis light).[21–23] UCNPs are considered as excellent materials for constructing optically controlled intelligent nano-systems, because they exhibit excellent luminescence properties and good physical and chemical properties,[24–26] and their luminescence properties can be flexibly regulated through an extended multi-shell structure.[27–29] In addition, functional modification of UCNPs through certain physical and chemical means can bind photosensitizers, hydrophilic groups, targeting groups or specific antibodies to their surface, thus realizing PDT in deep tissues, improving selectivity, and reducing side effects.[30–32] Additionally, P. Kowalik *et al.* discovered that upconversion nanomaterials ($NaYF_4$:20%Yb,0.2%Tm@SiO_2) excited at 980 nm can enable PDT without photosensitizers.[33] Therefore, a NIR-responsive multifunctional therapeutic platform can be realized *via* appropriate modification of UCNPs, which integrates functions including imaging, targeted drug delivery, and PDT in deep tissues.

Anionic drugs are an important part of the drug research and clinical treatment system, including short interfering RNA (siRNA), β-lactam antibiotics, polyoxometalates (POMs), and so on. A major issue limiting the use of anionic drugs lies in their highly negative charge, especially siRNA and POMs. Their charge not only blocks free diffusion across cell membranes but also risks repulsion by the anionic cell membrane surface. Thus, there is an urgent need for suitable carriers that can form stable complexes with anionic drugs, provide protection, ensure delivery to deep tissue, and bridge the gap between cell culture and animal models to enable efficient *in vivo* delivery of anionic drugs. Polyoxometalates (POMs) are a class of polyanionic clusters composed of discrete early transition metal oxides. Wells–Dawson POMs are one of the most classic archetypes of POM architectures, with the general formula $[X_2M_{18}O_{62}]^{n-}$ (X = heteroatom, *e.g.* P; M = metal atom, *e.g.* W).[34] This structure corresponds to an 18-nuclear heteropolyanion formed by the edge-sharing fusion of two trivacant Keggin-type fragments. Its central moiety features a belt-like framework composed of two tetrahedral XO_4 units, which is encircled by an array of 12 equatorial metal atoms. These metal atoms occupy the cores of MO_6 octahedra that are interconnected in an alternating pattern of corner-sharing and edge-sharing linkages. On either side of the central belt, three edge-sharing MO_6 octahedra assemble into a cap-like motif, which encapsulates the upper and lower facets of the overall framework, respectively.[35] Dawson-type POMs possess high thermal and chemical stability and show promise in the biomedical field due to their low cost, excellent redox properties, high thermal stability, and biocompatibility.[36,37] Based on the above advantages, POMs have become a hot research direction in many fields, such as anticancer therapy,[38] antibacterial treatment, anti-Alzheimer's disease research.[39] It has been found that POM inhibition can reduce Aβ-induced cytotoxicity by inhibiting Aβ aggregation through noncovalent interactions (hydrogen bonding, electrostatic attraction, hydrophobic interaction, π–π stacking, *etc.*), thereby affecting the physical and chemical properties of Aβ.[40–42] Furthermore, POMs, with their broad absorption spectrum and excellent chemical properties, can be used as photothermal agents, photocatalysts, and photosensitizers in combination with optical therapies to inhibit and depolymerize Aβ aggregation.[40,43] Li *et al.* found that POMs can generate ROS under UV irradiation, which oxidize Aβ to increase its hydrophilicity, thereby inhibiting Aβ aggregation and degrading Aβ oligomers.[44] However, the depth of penetration of UV light into tissues is limited, which makes it difficult to be applied to the treatment of brain diseases. Moreover, one of the important factors hindering the *in vivo* application of POMs is their poor targeting, which may easily interact with other physiological proteins before reaching the lesion site, resulting in toxic side effects and reduced therapeutic efficacy.

Chitosan (CH), a fully biodegradable and biocompatible natural polymer, is recognized as safe by the United States Food and Drug Administration (US FDA). Nanoparticles prepared from chitosan or its derivatives generally possess positively charged surfaces, which are excellent carriers for the anionic drugs.[45–48] Herein, we developed a NIR-responsive chitosan-modified UCNP nanocarrier system to deliver anionic drugs POMs. This strategy can enhance tissue penetration depth, achieve *in situ* excitation of POMs, reduce the toxic side effects of POMs, and improve the photo-oxidation inhibition and depolymerization of Aβ. In the above strategy, the UCNPs are three-layer core–shell upconversion materials, β-$NaYF_4$:Tm/Yb@$NaYF_4$@ $NaYF_4$:Er/Yb@$NaYF_4$ (denoted as UCNPs(Tm/Er)), which exhibit different photoresponses to low-power and high-power NIR light and can integrate imaging function and drug carriers into a single system. For these multi-shell upconversion nanomaterials, the inner $NaYF_4$ layer typically serves as an inert isolation layer and/or energy regulation layer, which separates the dopants into two different layers to maximize the efficiency of the upconversion processes as doping all of the lanthanide ions in one layer would lead to nonradiative energy transfers and lower upconversion efficiencies. The primary purpose of the outer $NaYF_4$ layer is to realize surface defect passivation, regulate energy transfer, and optimize luminescence dynamics. Under high-power NIR irradiation, UCNPs(Tm/Er) absorb NIR light and convert it to UV light to stimulate POMs to photo-oxidize Aβ, while under low-power NIR irradiation, they convert NIR to Vis light for imaging. In addition, we investigated the effects of the ratio of UCNPs@SiO_2@GPS@CH to POMs, pH value, and the degree of CH modification on the drug loading capacity of UCNPs@SiO_2@GPS@CH-POMs (denoted as UCNPs@CH-POMs). Subsequently, the ROS production with and without Aβ is also evaluated. This innovative design of a NIR-responsive multifunctional anionic drug carrier represents a significant breakthrough in photodynamic strategies for the potential alleviation of Aβ cytotoxicity.

2. Materials and methods

2.1. Materials

Rare earth chlorides ($YCl_3·6H_2O$, $YbCl_3·6H_2O$, $TmCl_3·6H_2O$, and $ErCl_3·6H_2O$) and sodium tungstate dihydrate ($Na_2WO_4·2H_2O$, 99.5%) were supplied by Aladdin Reagents (Shanghai, China). Phosphoric acid (H_3PO_4) was bought from Hongyan Reagent Factory (Tianjin, China). Potassium chloride (KCl) and hydrochloric acid (HCl) were sourced from Luoyang Chemical Reagent Factory and Yantai Shuangshuang Chemical Co., Ltd, respectively. 3-Aminopropyltriethoxysilane (APTES) and 2,4-dinitro-phenylhydrazine (DNPH) were bought from Maclean's (Shanghai, China). Sigma-Aldrich (St Louis, MO, USA) provided oleic acid, octadecene, (3-glycidyloxypropyl)trimethoxysilane (GPS), chitosan (CH, molecular weight: 190 000–300 000 Da), 1,3-diphenylisobenzofuran (DPBF), and 1,1,1,3,3,3-hexafluoro-2-propanol (HFIP). Aβ peptide was sourced from MedChemExpress (Shanghai, China). The DCFH-DA-based ROS kit was obtained from Beyotime Biotechnology (Shanghai, China). All other chemicals used were of analytical grade.

2.2. Synthesis of β-$NaYF_4$:Tm/Yb (UCNPs(Tm))

β-$NaYF_4$:Tm/Yb upconversion nanoparticles (UCNPs) were synthesized under a high-purity nitrogen atmosphere. First, an aqueous rare earth chloride solution containing 700 μL of 2 M YCl_3, 600 μL of 1 M $YbCl_3$, and 370 μL of 0.02 M $TmCl_3$ was added into a 100 mL round-bottom flask preloaded with 30 mL of 1-octadecene and 12 mL of oleic acid. Under nitrogen protection, water was removed *via* vacuum evaporation, and the mixture was gradually heated to 140 °C until a clear, homogeneous solution was obtained. Upon cooling the solution to 55 °C, a 10 mL methanol (MeOH) dispersion of ammonium fluoride (8 mmol) and sodium hydroxide (5 mmol) was added, and the mixture was stirred for 30 min. MeOH was then evaporated under vacuum at 55 °C. The reaction temperature was rapidly increased to 300 °C and held for 1.5 h. After cooling the mixture to 70 °C, excess ethanol (EtOH) was added, followed by centrifugation at 8000 rpm for 5 min to collect the β-$NaYF_4$:Tm/Yb UCNPs.

2.3. Synthesis of β-$NaYF_4$:Tm/Yb@$NaYF_4$

The synthesis of β-$NaYF_4$:Tm/Yb@$NaYF_4$ was conducted under a high-purity nitrogen atmosphere with a nitrogen flow rate of 60 mL min^{-1}. A 2 M YCl_3 aqueous solution (900 μL) was added to a mixed solution consisting of 30 mL 1-octadecene and 12 mL of oleic acid. The mixture was subjected to vacuum to remove water, and then gradually heated to 140 °C until a clear, homogeneous solution was obtained. After cooling the solution to 80 °C, an *n*-hexane dispersion of β-$NaYF_4$:Tm/Yb core nanoparticles (5 mL, 60 mg mL^{-1}) was added. Then, *n*-hexane was removed under vacuum and the temperature was raised to 140 °C. Upon cooling the solution to 55 °C, a MeOH dispersion (10 mL) containing 7 mmol ammonium fluoride and 4.4 mmol sodium hydroxide was added to the above mixture, followed by a 30-minute reaction.

2.4. Synthesis of β-$NaYF_4$:Tm/Yb@$NaYF_4$@$NaYF_4$:Er/Yb

A rare earth salt solution (1.4 mmol $YCl_3·6H_2O$, 0.35 mmol $YbCl_3·6H_2O$, and 0.035 mmol $ErCl_3·6H_2O$) was added to a mixed solution of 12 mL oleic acid and 30 mL 1-octadecene, at a stirring speed of 2000 rpm. The following steps are the same as those for synthesizing β-$NaYF_4$:Tm/Yb@$NaYF_4$ core–shell nanoparticles, with two key differences: the aforementioned $NaYF_4$:Tm/Yb@$NaYF_4$ nanoparticles serve as the core (5 mL, 60 mg mL^{-1}), and $NaYF_4$ epitaxial shell growth depends on the $YCl_3·6H_2O$ precursor.

2.5. Synthesis of β-$NaYF_4$:Tm/Yb@$NaYF_4$@$NaYF_4$:Er/Yb@$NaYF_4$

A rare earth salt solution (1.8 mmol $YCl_3·6H_2O$) was added into a mixed solution of 12 mL oleic acid and 30 mL 1-octadecene, and stirred thoroughly. The following steps are the same as those for synthesizing β-$NaYF_4$:Tm/Yb@$NaYF_4$ core–shell nanoparticles, with two key adjustments: the core material was replaced with β-$NaYF_4$:Tm/Yb@$NaYF_4$@$NaYF_4$:Er/Yb nanoparticles, and $YCl_3·6H_2O$ was employed as the precursor of epitaxial shell growth.

2.6. Synthesis of UCNPs(Tm/Er)@SiO_2 nanoparticles

UCNPs(Tm/Er) were coated with SiO_2 according to a previous study.[9] A 100 mL round-bottom flask was charged with 3.6 mL hexanol, 3.6 mL Triton X-100, and 14 mL cyclohexane, which were mixed thoroughly. Following this, 680 μL of water was added and stirred into the mixture. A suspension of 160 mg UCNPs(Tm/Er) in 2 mL cyclohexane was prepared and added to the reaction solution. With intensive stirring, 100 μL TEOS was subsequently introduced. After adding 160 μL ammonia to the mixture, the reaction was allowed to proceed for 24 h. The resulting UCNPs(Tm/Er)@SiO_2 was isolated by centrifugation at 8000 rpm for 5 min, and rinsed three times with EtOH and water sequentially.

2.7. Synthesis of UCNPs(Tm/Er)@SiO_2@GPS nanoparticles

50 mg UCNPs(Tm/Er)@SiO_2 was diffused in 10 mL of H_2O with ultrasonic treatment for 30 min. After that, 100 μL of (3-glycidylpropyloxy)trimethoxysilane (GPS) was added and continuously stirred for 24 h at room temperature. The obtained solution was condensed and refluxed at 70 °C for 2 h and then cooled to room temperature. The UCNPs(Tm/Er)@SiO_2@GPS were precipitated *via* centrifugation at 9000 rpm for 8 min at room temperature.

2.8. Synthesis of UCNPs(Tm/Er)@SiO_2@GPS@CH nanoparticles

100 mg UCNPs(Tm/Er)@SiO_2@GPS was ultrasonically dispersed in 10 mL of H_2O. Then, 100 μL of chitosan (CH) was added, and stirring was maintained at room temperature for 24 h. Afterward, the pH value of the obtained solution was tuned to weak alkalinity with a NaOH solution, and unreacted CH was separated *via* centrifugation. The precipitate was centrifugally washed with deionized water twice to obtain the UCNPs(Tm/Er)@SiO_2@GPS@CH.

2.9. Preparation of α-$K_6P_2W_{18}O_{62}\cdot14H_2O$ (POMs)

α-$K_6P_2W_{18}O_{62}\cdot14H_2O$ (POM) was synthesized according to the literature.[49] Under vigorous stirring, a solution of 150 g $Na_2WO_4\cdot2H_2O$ (0.455 mol) in 175 mL deionized water was acidified by adding 125 mL of 4 M HCl (0.50 mol) in fractions. Once the turbid solution became clear again, 125 mL of 4 M H_3PO_4 (0.50 mol) was slowly introduced, resulting in a pale yellow, clear solution. This solution was refluxed for at least 24 h, with the yellow color deepening noticeably over the reaction period. After cooling to room temperature, 75 g KCl was added to the solution, and the resulting precipitated solid was filtered and air-dried *via* aspiration. The crude product was dissolved in 325 mL of deionized water. Insoluble impurities were removed by filtration and the clear filtrate was heated to approximately 80 °C for at least 72 h, then cooled to room temperature and finally stored in a 4 °C refrigerator. After several days, well-crystallized yellow α-$K_6P_2W_{18}O_{62}\cdot14H_2O$ was harvested. POMs were dissolved in water to prepare POM solutions with concentrations of 6 mg mL^{-1}, 4 mg mL^{-1}, 3 mg mL^{-1}, and 2 mg mL^{-1}.

2.10. Preparation of UCNPs(Tm/Er)@SiO_2@GPS@CH-POMs (UCNPs@CH-POMs)

19 mg UCNPs(Tm/Er)@SiO_2@GPS@CH was dispersed in 5 mL of H_2O and ultrasonicated for 30 min. Then, 5 mL of POM solution (6 mg mL^{-1}, 4 mg mL^{-1}, 3 mg mL^{-1}, and 2 mg mL^{-1}) was added and stirred for 24 h at room temperature in the dark. The solution was centrifuged (12 000 rpm, 5 min) and the supernatant and UCNPs@CH-POMs were collected.

2.11. POM load assessment of UCNPs@CH-POMs

The control group was employed to establish a standard curve for the POM concentration–absorbance relationship. The solutions of the control group are POM solutions without a UCNPs@SiO_2@GPS@CH-POMs nanocarrier. They were prepared by diluting 1 mL of POM solutions (6 mg mL^{-1}, 4 mg mL^{-1}, 3 mg mL^{-1}, and 2 mg mL^{-1}) with 1 mL of deionized water to achieve a 1 : 1 dilution. The experimental group was used for the detection of drug release behavior. For this group, at predetermined time points, the supernatant was obtained by centrifuging the UCNPs@SiO_2@GPS@CH-POM drug-loading system at 12 000 rpm for 5 minutes, and the resulting supernatant was then used as the test solution. The two groups were diluted by the same factor, and the UV-Vis absorption spectra were collected five times respectively. The loading x of POMs per mg of UCNPs@SiO_2@GPS@CH nanoparticles was calculated using eqn (1).

$$X = \frac{(\rho_1 - \rho_2) \times \frac{V_1}{V_2} \times (V_2 + V_3)}{M} \quad (1)$$

Here, ρ_1 and ρ_2 are the average values of the mass concentrations corresponding to the absorption peaks of the control group and the experimental group, V_1 is the total volume of the reaction solution, V_2 is the volume of the solution taken out during dilution, V_3 is the volume of deionized water added during dilution, and M is the mass of UCNPs.

The utilization rate of POMs after drug loading reaction is calculated using eqn (2).

$$\text{Utilization ratio of drugs} = \frac{\text{Total dosage} - \text{Drug loading}}{\text{Total dosage}} \quad (2)$$

2.12. POM release assessment of UCNPs@CH-POMs

Ultrasonic dispersion of UCNPs@CH-POMs in 2 mL H_2O or PBS buffer. After 5 min, it was centrifuged (12 000 rpm, 1 min) and the supernatant was taken to record the UV-Vis absorption spectrum. After this, the supernatant was put back into the drug-loading system of UCNPs@CH-POMs and the above operations were repeated until the peak value of the UV-Vis absorption spectrum did not increase significantly.

2.13. Preparation of Aβ solution

A human $A\beta_{1-42}$ (Aβ) monomer (1 mg) was dispersed in 1 mL hexafluoroisopropanol (HFIP), and then oscillated at 4 °C for 2 h for further dissolution. The solution was stored as a stock at −20 °C. The HFIP was evaporated with a gentle nitrogen stream when it was used, and then mixed in an equal volume of deionized water to prepare the Aβ solution.[50] This solution was oscillated for 1 min and then incubated at 37 °C for 1 day to induce Aβ fibril formation.

2.14. Evaluation of reactive oxygen species generation

In the experiment, different groups were prepared by mixing 5 mg of UCNPs(Tm/Er)@SiO_2@GPS@CH-POMs, 1 μL of Aβ fibril solution (240 μM), and 1 μL of DCFH-DA (10 μM) in 500 μL of phosphate buffer. The solution was homogenized for approximately 1 minute at room temperature using a vortex mixer. Following irradiation with a 980 nm laser (3.10 W cm^{-2}), fluorescence measurements were taken every 5 min over 30 min at 525 nm (excited at 488 nm) using a fluorescence spectrophotometer (FLS1000, UK). In this study, 2,7-dichlorofluorescein diacetate (DCFH-DA) was employed as a probe for detecting reactive oxygen species (ROS). Upon excitation of UCNPs(Tm/Er)@SiO_2@GPS@CH-POMs by a 980 nm laser, ROS are generated, which oxidize DCFH to form dichlorofluorescein (DCF). The fluorescence intensity of DCF exhibits a positive correlation with ROS levels. DCF emits a characteristic fluorescence signal at 525 nm when excited at 488 nm, and this optical parameter was used for the quantitative analysis of DCF *via* a fluorescence spectrophotometer. In this experiment, a 980 nm laser was used to generate ROS, while 488 nm light served as the excitation source for DCF fluorescence.

2.15. Evaluation of singlet oxygen generation

1,3-Diphenylisobenzofuran (DPBF) is a $^1O_2$ fluorescent probe. $^1O_2$ oxidizes DPBF, resulting in reduced absorption of DPBF at 410 nm. For the experiment, various sample groups were prepared by combining 10 μL of 1 mg mL^{-1} POMs, 5 mg of UCNPs(Tm/Er)@SiO_2@GPS@CH, and 2 μM Aβ (fibrils or

monomers), and 50 μM DPBF in 500 μM DMSO. These sample sets were vortex-mixed for approximately 1 minute at room temperature to ensure thorough mixing. After irradiation with a 980 nm laser (3.10 W cm^{-2}), the absorption intensity of DPBF was recorded every 5 min for a total of 30 min using a UV–Vis spectrophotometer (UV-1700).

3. Results and discussion

3.1. Characterization of UCNPs(Tm/Er)

In this study, we gradually synthesized three-layer core–shell upconversion nanoparticles (UCNPs(Tm/Er)) by a co-precipitation method. The illustration of the UCNPs(Tm/Er) structure is shown in Fig. 1a. A transmission electron microscope (TEM) and ImageJ were used to characterize and analyze the crystal morphology and particle size distribution of the nanoparticles at each stage. As shown in Fig. 1b–e, the β-$NaYF_4$:Tm/Yb core nanoparticles exhibit a nearly ellipsoid shape with a uniform morphology. After being coated with the first $NaYF_4$ shell, the $NaYF_4$:Tm/Yb@$NaYF_4$ core–shell nanoparticles exhibit a capsule-like morphology with uniform particle size and good monodispersity. By randomly measuring a number of particles, the statistical plots of particle size distribution were obtained, as summarized in Fig. S1 and Fig. S2. It can be seen that the particle size of UCNPs increases gradually with the increase in the number of shell layers. The average length and width of UCNPs(Tm/Er) are 86 ± 1 nm and 45 ± 2 nm, respectively. After the β-$NaYF_4$:Tm/Yb core nanoparticles are coated with three layers, their width increases by approximately 13 nm, while their length increases by about 48 nm. This indicates that the growth rate along the [001] crystal plane is higher than that along the [100] crystal plane. The high-resolution TEM image (Fig. 1f), electron diffraction pattern (Fig. 1g), and X-ray diffraction pattern (Fig. 1h) show that UCNPs(Tm/Er) are hexagonal β crystal structures. Fig. 1i shows the upconversion luminescence spectra of UCNPs(Tm/Er) upon irradiation with NIR light, including low-power density (15 W cm^{-2}) and high-power density (500 W cm^{-2}). The upconversion luminescence mechanism of UCNPs(Tm/Er) is described as follows: Y^{3+} absorbs 980 nm light, followed by energy transfer from Yb^{3+} ions to Tm^{3+} or Er^{3+} ions.[9,33] Under low-power NIR excitation (Fig. 1j), UCNPs(Tm/Er) exhibit characteristic upconversion luminescence originating from Er^{3+} ions. Under high-power NIR excitation (Fig. 1k), UCNPs(Tm/Er) exhibit upconversion luminescence due to both Tm^{3+} and Er^{3+} ions. Emission peaks at 347, 365, 450, and 475 nm are attributed to the characteristic f–f transitions of Tm^{3+} ions ($^1I_6 \rightarrow {}^3F_4$, $^1D_2 \rightarrow {}^3H_6$, $^1D_2 \rightarrow {}^3F_4$, $^1G_4 \rightarrow {}^3H_6$, respectively). Emissions centered at 409, 520, and 540 nm are due to the characteristic f–f transitions of Er^{3+} ions ($^4H_{9/2} \rightarrow {}^4I_{15/2}$, $^4H_{11/2} \rightarrow {}^4I_{15/2}$, and $^4S_{3/2} \rightarrow {}^4I_{15/2}$, respectively).

In order to improve the water solubility of nanoparticles, a silica shell was coated on UCNPs(Tm/Er) to get UCNPs(Tm/Er)@SiO_2 by the microemulsion method. UCNPs(Tm/Er)@SiO_2 were characterized by TEM, Fourier transform infrared spectroscopy (FTIR), and energy dispersive spectroscopy (EDS). As shown in Fig. 2a, the TEM image indicates that the silica-coated nanoparticles remain a capsule-like morphology with good monodispersity. A further magnified TEM image (Fig. 2b) shows a uniformly coated silica layer with a thickness of approximately 10 nm. Moreover, EDS elemental mapping images of UCNPs(Tm/Er)@SiO_2 (Fig. 2c and d) confirmed the presence of O, F, Na, Si, Y, Er, Tm, and Yb, and their mass percentages were also analyzed (Fig. S3 and Table S1). These results indicate the successful preparation of UCNPs(Tm/Er)@SiO_2.

Before coating CH onto the surface of UCNPs(Tm/Er)@SiO_2, GPS was employed to introduce epoxy groups onto the nanoparticle surface. According to the dynamic light scattering (DLS) analysis results (Fig. 3a), the hydrodynamic diameter of the nanoparticles exhibited a slight increase after being coated with the silica layer and functionalized with GPS. Subsequently, the grafting of CH onto the surface of UCNPs(Tm/Er)@SiO_2 resulted in a significant increase in the hydrodynamic diameter (about 345 nm) attributed to the high molecular weight of CH (190 000–300 000 Da). Thermogravimetric analysis (TGA) was employed to further characterize the surface modification. As shown in Fig. 3b, the weight loss of UCNPs(Tm/Er) was approximately 17% because of the anchored oleic acid ligands on the surface. After SiO_2 coating, the weight of UCNPs(Tm/Er)@SiO_2 decreases to 96% at 100 °C, which is attributed to the evaporation of adsorbed H_2O. The final weight of UCNPs(Tm/Er)@SiO_2 remains stable at 95%, corresponding to an actual weight loss of about 1%. Similarly, the weight loss of UCNPs(Tm/Er)@SiO_2@GPS and UCNPs(Tm/Er)@SiO_2@GPS@CH is approximately 3% and 5%, respectively. In the FTIR spectra (Fig. 3c), the characteristic vibrational signals of oleic acid in UCNPs(Tm/Er) (–CH_3: 2927 cm^{-1}, 2850 cm^{-1}; –C═O: 1352 cm^{-1}, 1593 cm^{-1}) were absent following SiO_2 coating. Furthermore, two new FTIR bands at 797 cm^{-1} and 1083 cm^{-1} were observed, which are attributed to the symmetric and asymmetric stretching vibrations of the Si–O–Si bond, respectively. After the surface of UCNPs(Tm/Er)@SiO_2 was modified with GPS, a broad band with weak absorption intensity appeared in the FTIR spectrum at the 666 cm^{-1} band, which was caused by the out-of-plane bending vibration of C–OH on GPS. Further surface modification with CH introduces a new band at 770 cm^{-1} which is caused by the distortion of N–H in NH_2. These results indicate that GPS and CH have been successfully modified on the surface of UCNPs(Tm/Er)@SiO_2.

In addition, the surfaces of UCNPs(Tm/Er), UCNPs(Tm/Er)@SiO_2, UCNPs(Tm/Er)@SiO_2@GPS, and UCNPs(Tm/Er)@SiO_2@GPS@CH are detected by X-ray photoelectron spectroscopy (XPS) (Fig. 3d and Fig. S4). The C 1s spectrum of UCNPs(Tm/Er) (Fig. S4a) exhibits four peaks at 282.8, 284.9, 286.1, and 288.7 eV, corresponding to the C–OOH, C–C, C–OH/C–O–C, and O–C═O groups of oleic acid, respectively. Similarly, the C 1s spectra of UCNPs(Tm/Er)@SiO_2 (Fig. S4d), UCNPs(Tm/Er)@SiO_2@GPS (Fig. S4g), and UCNPs(Tm/Er)@SiO_2@GPS@CH (Fig. S4j) display peaks analogous to those of UCNPs(Tm/Er). Furthermore, in the C 1s spectrum of UCNPs(Tm/Er)@SiO_2@GPS

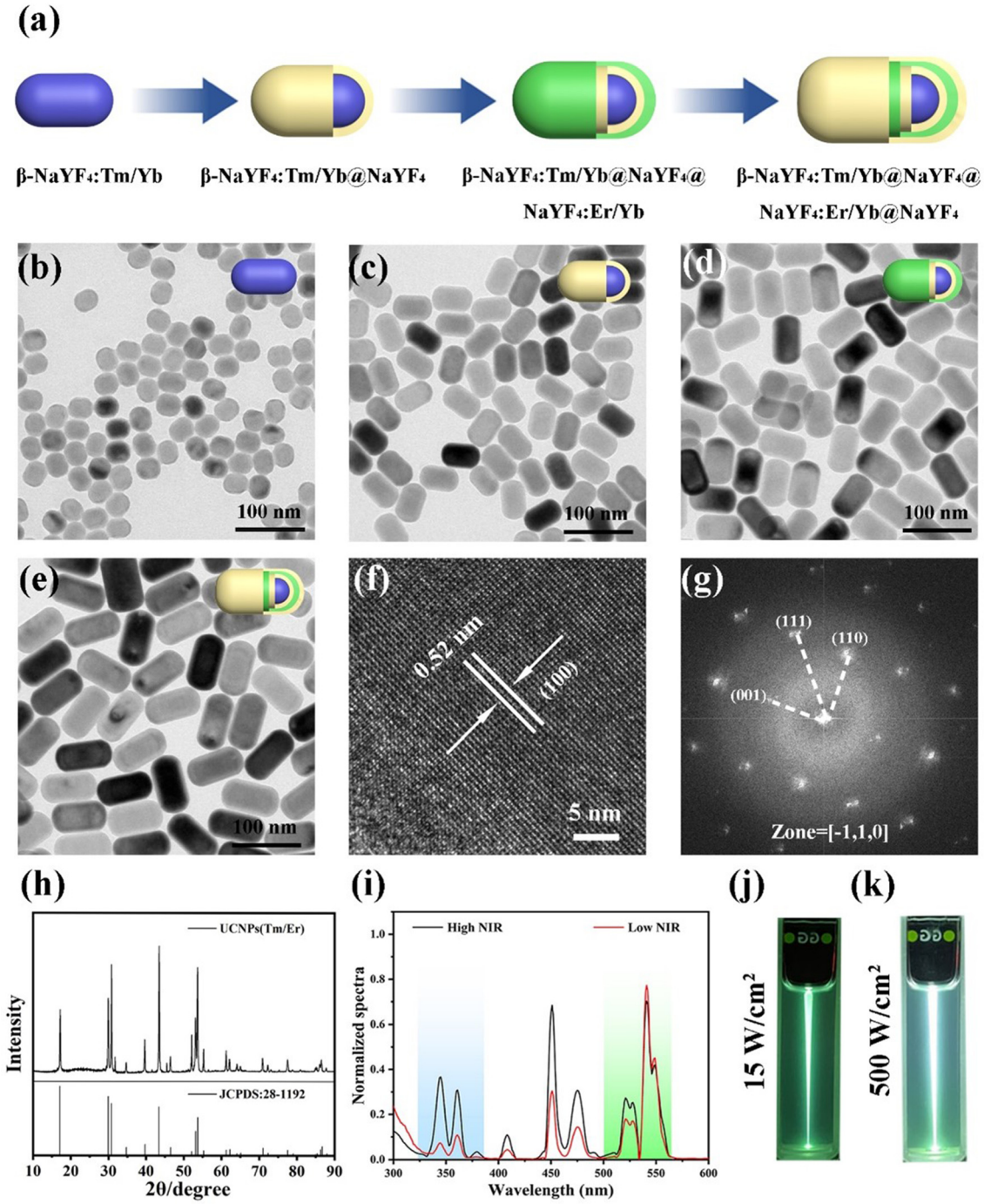

Fig. 1 (a) Schematic diagram of the core–shell structure of UCNPs(Tm/Er). TEM images of (b) $NaYF_4$:Yb/Tm, (c) $NaYF_4$:Yb/Tm@$NaYF_4$, (d) $NaYF_4$:Yb/Tm@$NaYF_4$@$NaYF_4$:Yb/Er, and (e) $NaYF_4$:Yb/Tm@$NaYF_4$@$NaYF_4$:Yb/Er@$NaYF_4$ (UCNPs(Tm/Er)). (f) High-resolution electron microscopy image, (g) electron diffraction pattern, and (h) XRD pattern of UCNPs(Tm/Er). (i) Normalized upconversion emission spectra of UCNPs(Tm/Er) under 980 nm NIR light excitation. Photograph of UCNPs(Tm/Er) with the irradiation of (j) low-power NIR light (15 W cm^{-2}) and (k) high-power NIR light (500 W cm^{-2}).

and UCNPs(Tm/Er)@SiO_2@GPS@CH, the relative intensity of the C–OH/C–O–C peak at 286.2 and 286.1 eV increases, which is attributed to the epoxide groups of GPS and hydroxyl (–OH) groups of CH, respectively. The Si 2p spectrum of UCNPs(Tm/Er) show no peaks (Fig. S4b), while a strong peak at 103.5 eV appears in the high-resolution Si 2p spectrum of UCNPs(Tm/Er)@SiO_2 (Fig. S4e). This peak is attributed to the O–Si–O groups in the silica shell, confirming the successful synthesis of UCNPs(Tm/Er)@SiO_2. As shown in Fig. S4h and S4k, strong peaks at 103.5 eV also appear in the Si 2p spectra of UCNPs(Tm/Er)@SiO_2@GPS and UCNPs(Tm/Er)@SiO_2@GPS@CH, but the peak intensity of UCNPs(Tm/Er)@SiO_2@GPS@CH is slightly lower due to the

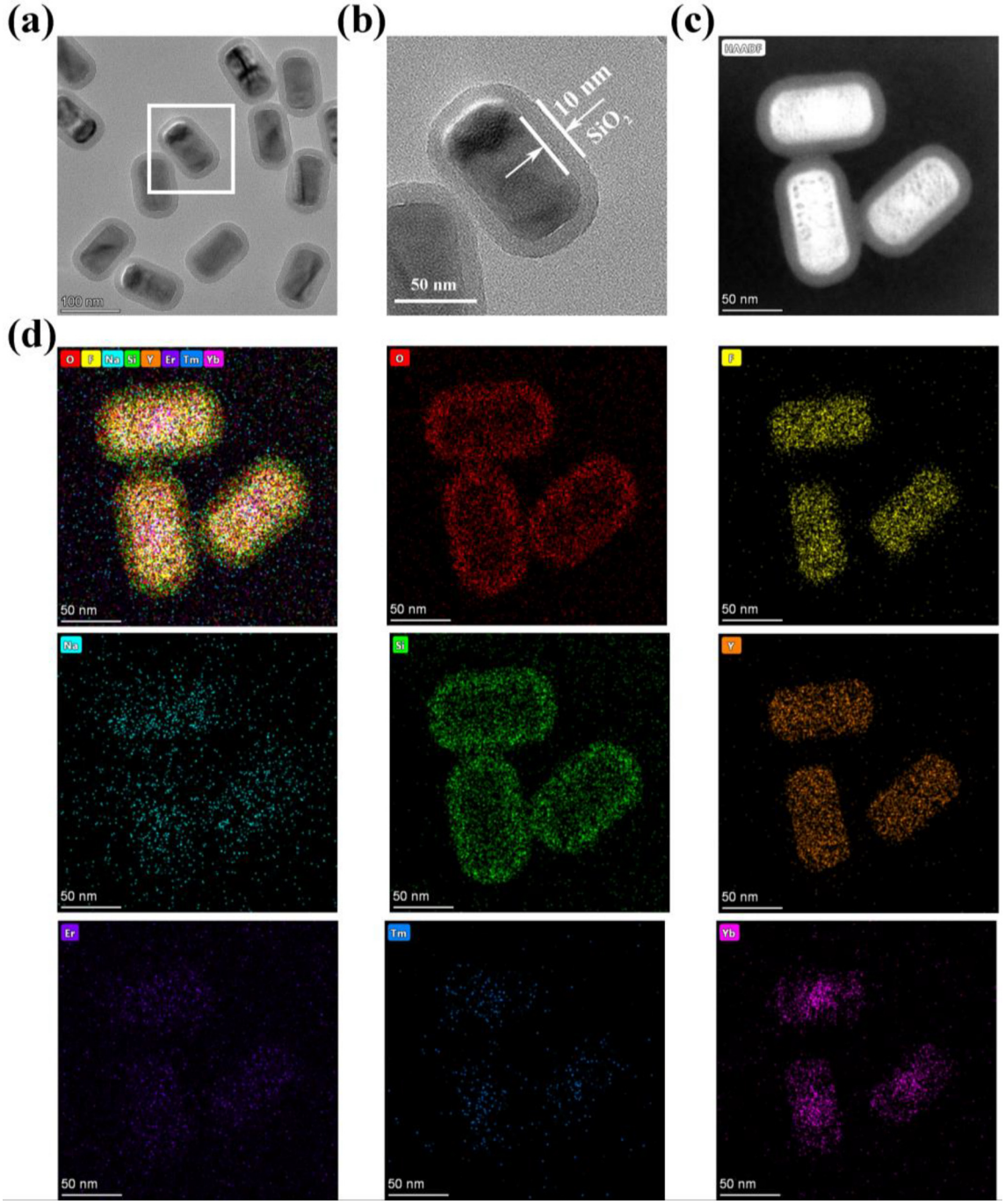

Fig. 2 (a) TEM images of UCNPs(Tm/Er)@SiO_2, (b) magnified image of the area marked by the white square in (a). (c and d) EDS maps of O, F, Na, Si, Y, Er, Tm, and Y elements in UCNPs (Tm/Er)@SiO_2.

masking effect of its CH shell. The N 1s spectra of UCNPs(Tm/Er), UCNPs(Tm/Er)@SiO_2, and UCNPs(Tm/Er)@SiO_2@GPS show no peaks (Fig. S4c, S4f and S4i). For UCNPs(Tm/Er)@SiO_2@GPS@CH, its N 1s spectrum (Fig. S4l) exhibits two peaks at 399.9 eV and 402.2 eV, assigned to the $-NH_2$ and protonated $-NH^{3+}$ groups of CH, respectively. These XPS data verify that UCNPs(Tm/Er) were first successfully coated with SiO_2, then functionalized with GPS, and finally modified with CH.

In the following experiments, only UCNPs(Tm/Er)@SiO_2@GPS@CH was used for loading POMs. In subsequent descriptions, UCNPs(Tm/Er)@SiO_2@GPS@CH is abbreviated as UCNPs@CH.

3.2. Enhancement of POM loading performance on UCNPs@CH

The structure of POMs was characterized *via* FTIR. Compared with previous literature, the FTIR results (Fig. S5 and Table S2)

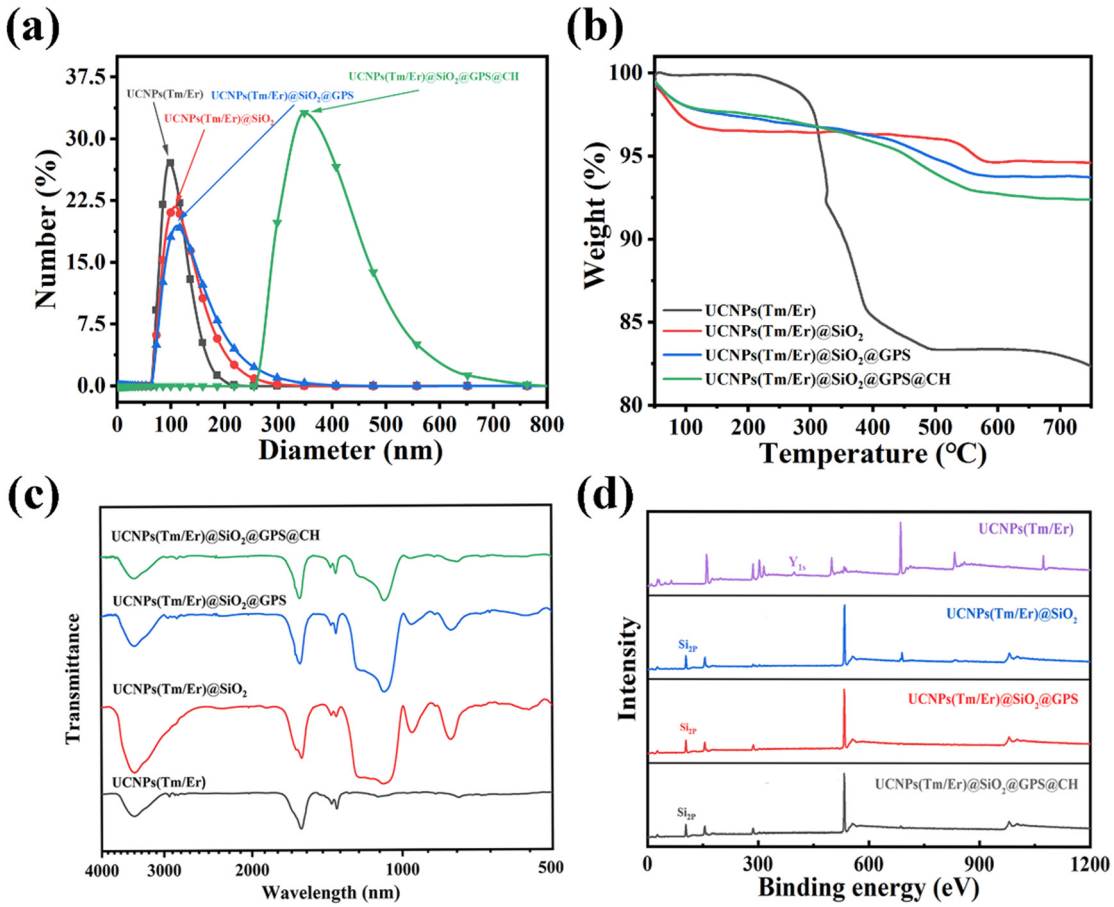

Fig. 3 (a) Hydrodynamic particle size distribution determined by dynamic light scattering (DLS), (b) thermogravimetric analysis plots, (c) FTIR spectra, and (d) XPS spectra of UCNPs(Tm/Er), UCNPs(Tm/Er)@SiO_2, UCNPs(Tm/Er)@SiO_2@GPS, and UCNPs(Tm/Er)@SiO_2@GPS@CH.

demonstrated that Dawson-structured POMs were successfully synthesized. The UV-Vis absorption spectra of POM solutions with different concentrations (0.048–0.24 mg mL^{-1}) are presented in Fig. S6. Based on the absorbance and corresponding mass concentration of POMs at the maximum absorption peak (λ = 295 nm), a standard curve of POMs in deionized water was constructed (Fig. 4a). Within the concentration range of 0.048–0.24 mg mL^{-1}, the correlation coefficient (R^2) is close to 1, confirming a strong linear relationship between POM concentration and absorbance. Consequently, the linear regression equation derived from this curve can be employed to quantify the concentration of POMs in solution. The POM loading capacity of UCNPs@CH is further determined by comparing the UV-Vis absorption spectra of the solution before and after the loading process.

In the initial POM loading experiment, the concentrations of POMs and UCNPs@CH were set to 1 mg mL^{-1} and 0.03 mg mL^{-1}, respectively. As shown in Fig. S7, the UV-Vis absorption spectra of the supernatant before and after the POM-loading process are nearly identical, with minor differences likely arising from operational or instrumental errors. This result indicates two possibilities: either POMs do not absorb onto UCNPs@CH or the amount of adsorbed POMs is too low to be detected. To optimize the POM-loading conditions, the dosages of POMs and UCNPs@CH nanoparticles were increased in the subsequent experiments, where their concentrations were adjusted to 6 mg mL^{-1} and 2 mg mL^{-1}, respectively. However, the UV-vis spectra of the supernatant before and after the POM loading remained similar (Fig. S8), indicating that POMs do not adsorb onto UCNPs@CH. Theoretically, the negatively charged POMs should adsorb onto positively charged UCNPs@CH *via* electrostatic interactions. Thus, we hypothesize that the quantity of CH on UCNPs@CH is insufficient to load POMs. In subsequent experiments, we aim to increase the CH content on UCNPs@CH during the modification process.

3.2.1. pH adjustment for UCNPs@CH purification and optimization of POM loading performance. The high-water solubility of CH molecules under weakly acidic conditions prevents the centrifugal separation of UCNPs@CH, which may thus remain in the supernatant. To address this issue, after modifying UCNPs@SiO_2@GPS with CH, the solution pH was adjusted to a weakly alkaline value prior to centrifugal separation. The resulting UCNPs@CH was then used for POM loading. As shown in Fig. S9, the UV-Vis absorption spectra of the supernatants before and after the drug-loading process

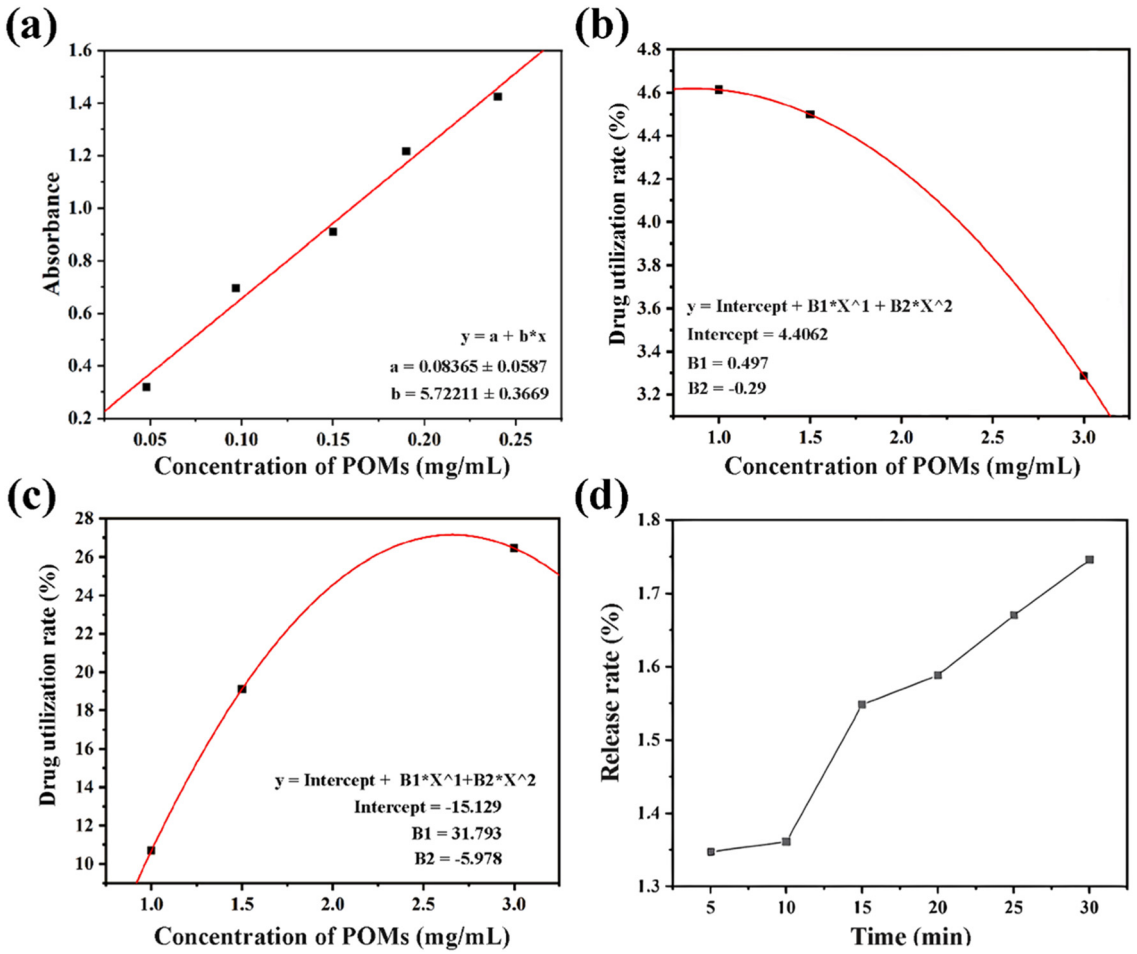

Fig. 4 (a) Standard curve of POMs in deionized water. (b) Fitting curve of the POM utilization rate at different concentrations after increasing CH content on UCNPs@CH *via* weakly alkaline pH adjustment. (c) Fitting curve of the POM utilization rate at different concentrations after the two-step CH modification. (d) POM release curve of UCNPs@CH-POMs prepared with 3.0 mg mL^{-1} POMs.

were significantly different, indicating the successful loading of POMs onto UCNPs@CH. The POM loading capacity of UCNPs@CH at different POM concentrations was calculated using eqn (1). The results are summarized in Table 1. These data indicate that the POM loading capacity of UCNPs@CH increased with increasing POM concentration, and optimal loading was achieved when the POM concentration reached 3.0 mg mL^{-1}. Additionally, the POM utilization rates were calculated *via* eqn (2), and the corresponding curve (Fig. 4b) was fitted. The curve reveals that the POM utilization rate decreased as the POM concentration increased. Thus, further increasing the POM loading capacity of UCNPs@CH by raising the POM concentration is impractical, as this approach would lead to significant POM waste.

Table 1 POM loading amount on UCNPs@CH after pH-adjusted purification

Concentration of POMs (mg mL^{-1})	POM loading amount on UCNPs@CH (μg mg^{-1})
3.0	51.903
1.5	35.52
1.0	24.28

3.2.2. Enhancement of the CH modification level on UCNPs@CH and optimization of POM loading performance. Since POM loading is determined by the positively charged CH on UCNPs@CH, the extent of CH modification on UCNPs@CH is identified as the second factor influencing POM loading, following pH adjustment. To enhance CH content, a secondary CH modification step was introduced. The increase in CH content is expected to provide more interaction sites between POMs and UCNPs@CH. Experimental results after the two-step CH modification are presented in Fig. S10 and Fig. 4c, and the calculated POM loading capacities are summarized in Table 2. A comparison between Table 1 and Table 2 reveals a significant enhancement in POM loading capacity after the second CH modification. At POM concentrations of 3.0, 1.5, and 1.0 mg mL^{-1}, the loading capacity increased by 8.0, 4.2, and 2.3 times, respectively. These results confirm that multiple CH modification cycles are a feasible strategy to improve POM loading on UCNPs@CH. Additionally, the POM utilization

Table 2 POM loading amount on UCNPs@CH after the two-step CH modification

Concentration of POMs (mg mL^{-1})	POM loading amount on UCNPs@CH (μg mg^{-1})
3.0	415.41
1.5	149.56
1.0	55.66

curve (Fig. 4c) shows that the utilization rate increases with rising POM concentration.

To evaluate whether the POM delivery system leaks POMs, the supernatants of UCNPs@CH-POMs were analyzed *via* UV-Vis absorption spectra every five minutes (Fig. S11). The absorbance values showed a slight increase. As shown in the drug release rate plot (Fig. 4d), the release rate of POMs is very low, which indicates that POMs in the UCNPs@CH-POMs system are relatively stable. This stability is advantageous, as it allows UCNPs@CH-POMs to reduce the toxic side effects caused by the binding of free POMs to proteins during the delivery process.

3.3. Evaluation of ROS generation by NIR-irradiated UCNPs@CH-POMs

The photooxidative capacity of UCNPs@CH-POMs is hypothesized to be pivotal for inhibiting Aβ fibrillation and disassembling preformed Aβ fibrils, primarily by the production of ROS including hydroxyl radicals ($^{\bullet}$OH) and $^{1}O_2$. To evaluate the photooxidative capacity of UCNPs@CH-POMs under different conditions, 2′,7′-dichlorofluorescein diacetate (DCFH-DA) and 1,3-diphenylisobenzofuran (DPBF) were used as probes to quantify total ROS and $^{1}O_2$, respectively.

DCFH-DA itself is non-fluorescent. In the presence of ROS, it is oxidized to DCF (2′,7′-dichlorofluorescein), which emits green fluorescence (524 nm) under 488 nm excitation light. The DCFH-DA kit was therefore used to verify whether UCNPs@CH-POMs can generate ROS, which is an essential prerequisite for photodynamic therapy of AD. As shown in Fig. S12, the fluorescence intensity of DCF at 524 nm barely increased in the UCNPs@CH-POM solution under dark conditions, indicating negligible ROS production. In contrast, under NIR light irradiation (Fig. 5a and b), the fluorescence intensities of DCF in the UCNPs@CH-POM group and

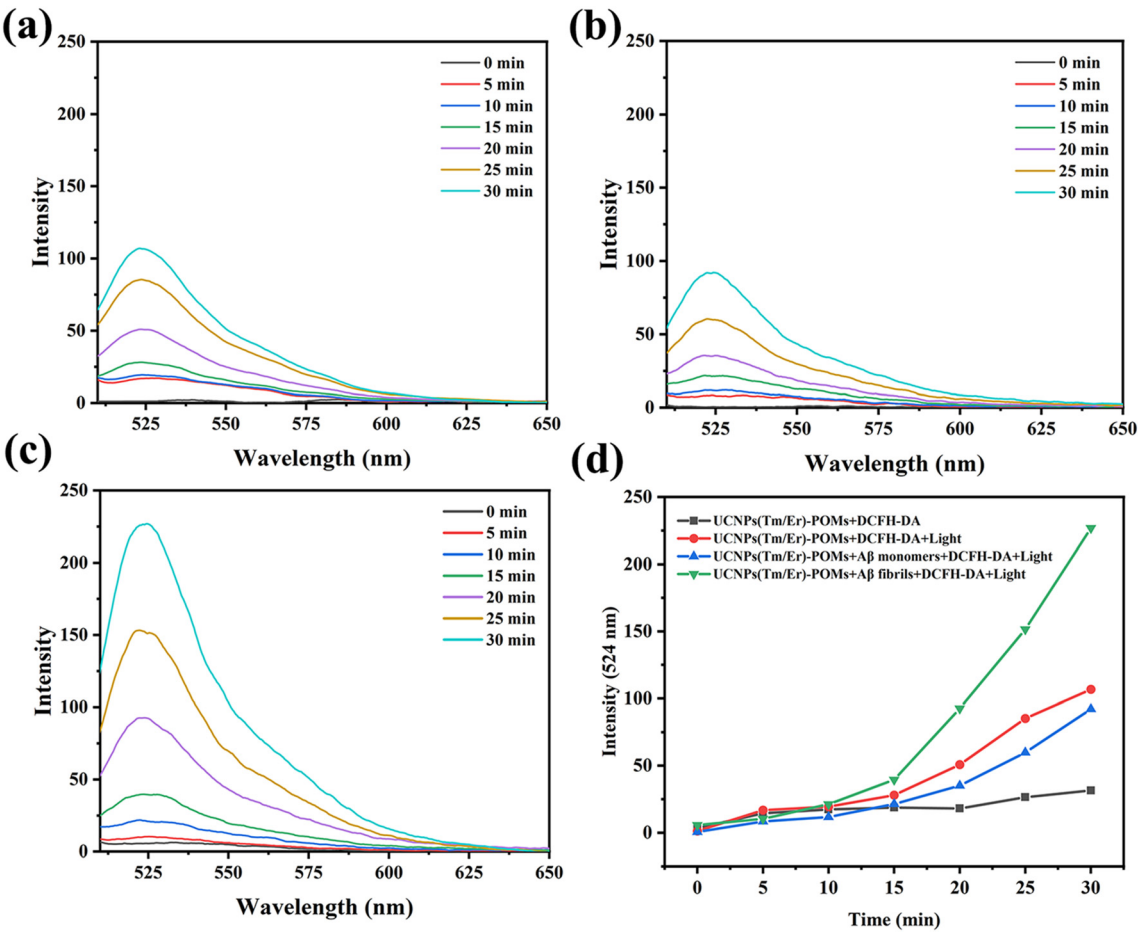

Fig. 5 Fluorescence spectra of DCF in the solution of (a) UCNPs@CH-POMs + DCFH-DA, (b) UCNPs@CH-POMs + Aβ monomers + DCFH-DA, and (c) UCNPs@CH + POMs + Aβ fibrils + DCFH-DA with NIR irradiation for a certain time. (d) The time-dependent fluorescence intensity profiles at 524 nm for all four experimental groups.

UCNPs@CH-POMs with Aβ monomer group exhibited similar increasing rates and trends. This indicates that UCNPs@CH-POMs can produce ROS under NIR irradiation and that Aβ monomers have no effect on ROS production. Notably, the fluorescence intensity of DCF at 524 nm in the UCNPs@CH-POM with Aβ fibril group was significantly enhanced after NIR light irradiation (Fig. 5c). Given that the isoelectric point (pI) of Aβ is about 5.3, Aβ fibrils exhibit a negatively charged surface that can interact with CH through electrostatic and hydrophobic interactions. We hypothesized that the Aβ fibrils may serve as nanoscale surfaces for the accumulation of UCNPs@CH-POMs. This accumulation could enhance the utilization of the UV light emitted by the UCNPs, thereby promoting increased ROS production.

Fig. 5d presents the time-dependent fluorescence intensity profiles at 524 nm for all four experimental groups. Within the first 15 minutes, there was almost no difference in fluorescence intensity among the groups. However, distinct differences emerged after 15 minutes. Compared with the Aβ monomer group, the UCNPs@CH-POM with Aβ fibril group exhibited a more pronounced ROS generation effect. These results indicate that for PDT using UCNPs@CH-POMs, irradiation with 980 nm NIR light for more than 15 minutes is required to achieve a significant therapeutic effect.

In summary, the photodynamic effect of UCNPs@CH-POMs leads to the generation of large amounts of ROS at the site of Aβ aggregates, which is capable of oxidizing and disassembling the aggregates. In regions without Aβ aggregates, ROS production is minimal, avoiding significant damage to normal cells. Thus, UCNPs@CH-POMs can alleviate Aβ fibril-induced neurotoxicity and reduce drug-related side effects, making it a promising candidate for PDT in AD.

Singlet oxygen ($^1O_2$), an important type of ROS, can depolymerize Aβ aggregates but has an extremely short half-life (10–320 ns). DPBF can be rapidly oxidized by $^1O_2$ to an endoperoxide, which further decomposes into 1,2-dibenzoylbenzene. This reaction reduces the absorbance peak of DPBF. The extent of $^1O_2$ generation is directly proportional to the decrease in the absorption intensity of DPBF.

Under 980 nm NIR irradiation (3.10 W cm^{-2}), UV-Vis absorption spectra of DPBF solutions were measured every 5 minutes, and were used as a control group. In the control group, the absorbance of DPBF at 417 nm did not decrease obviously, indicating that DPBF did not decompose under NIR irradiation (Fig. 6a). Similarly, the DPBF with POM group also exhibited no notable change in 417 nm absorbance under NIR irradiation, confirming negligible $^1O_2$ generation (Fig. 6b). The absorbance decrease at 417 nm in Fig. 6c was nearly identical to that in the control group, suggesting that UV light emitted by UCNPs (upon NIR absorption) failed to efficiently activate POMs to produce $^1O_2$. Notably, UCNPs@CH-POMs incubated with Aβ fibrils demonstrated higher $^1O_2$-generating capacity than those incubated with Aβ monomers under identical conditions (Fig. 6d and e). The slope of the absorbance decay

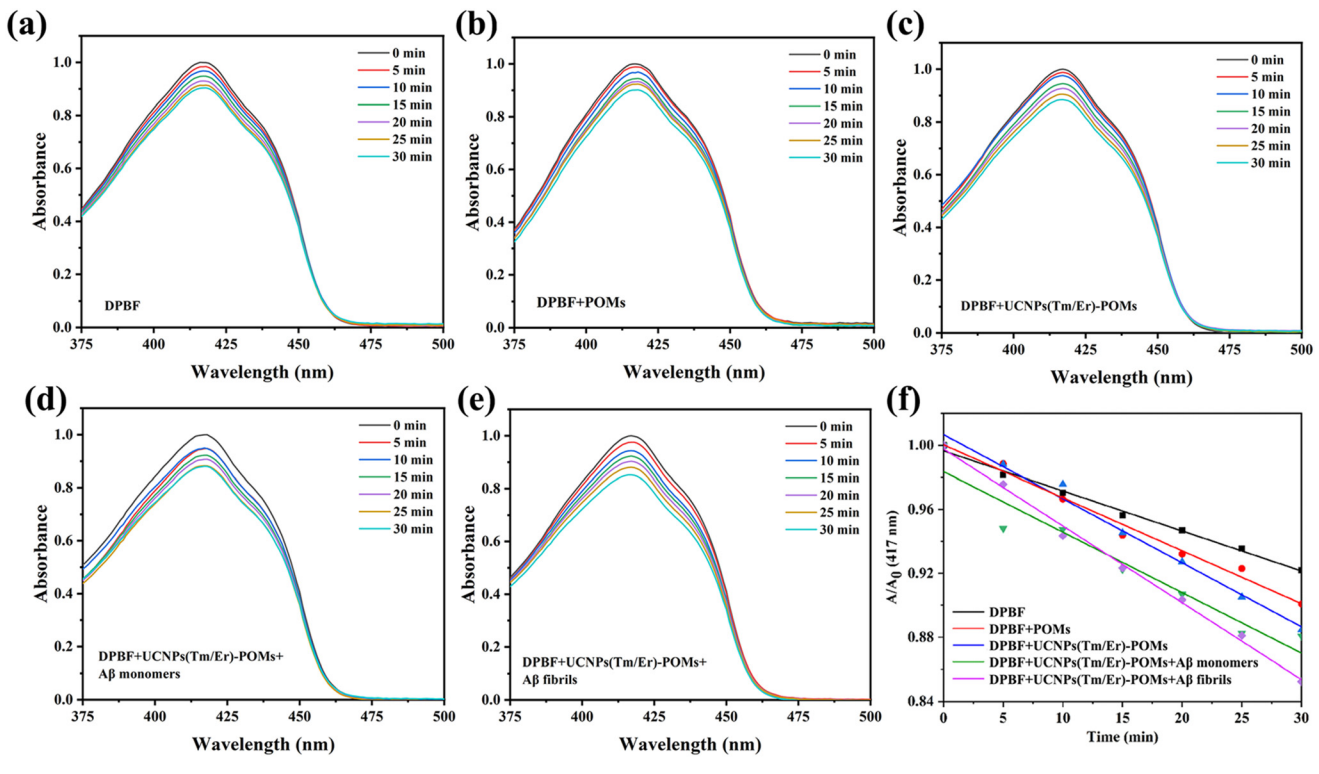

Fig. 6 UV-Vis absorption spectra of (a) DPBF, (b) DPBF + POMs, (c) DPBF + UCNPs@CH-POMs, (d) DPBF + UCNPs@CH-POMs + Aβ monomers, and (e) DPBF + UCNPs@CH-POMs + Aβ fibrils were measured after NIR irradiation every 5 minutes in DMSO. (f) The time-dependent fluorescence intensity profiles at 417 nm for all five experimental groups.

curve (Fig. 6f) reflects the capacity of yielding $^1O_2$. Compared to the control group, other groups showed minimal slope changes, indicating low $^1O_2$ production overall. While these results do not definitively confirm effective Aβ fibril depolymerization by UCNPs@CH-POMs, they demonstrate a more robust and stable photodynamic effect on Aβ fibrils relative to monomers.

ROS includes $^1O_2$, hydroxyl radical ($^{\bullet}OH$), and superoxide anions ($^{\bullet}O_2^-$). Comparing the detection results of ROS and $^1O_2$, significant ROS production was observed, whereas $^1O_2$ generation was negligible. This suggests that the primary ROS generated by the UCNPs@CH-POM system is not likely to be $^1O_2$ but other reactive oxygen species, such as $^{\bullet}OH$ or $^{\bullet}O_2^-$.

4. Conclusion

In conclusion, we successfully developed a multishelled NIR-responsive upconversion nanoplatform, UCNPs(Tm/Er)@SiO_2@GPS@CH, and systematically explored its performance as an anionic drug carrier using POMs as the model drug. The resulting UCNPs@CH-POM drug-loaded system exhibited a uniform capsule-like morphology, excellent monodispersity, and unique NIR-tunable luminescence (wavelength and color adjustable *via* NIR irradiation power), confirming its potential as a light-controlled intelligent nanocarrier. For POM loading, experimental data revealed a positive correlation between the CH modification level and POM loading capacity, which was attributed to electrostatic interactions between negatively charged POMs and positively charged CH. In the absence of 980 nm NIR irradiation, the UCNPs@CH-POM system remained stable in solution, minimizing POMs-related side effects during delivery and improving POM utilization at target sites. Under 980 nm NIR irradiation, the system triggered a photodynamic effect, generating abundant ROS that may efficiently depolymerize preformed Aβ fibrils and inhibit Aβ fibrillation. Notably, Aβ fibrils promoted ROS generation by providing nanoscale surfaces for the accumulation of UCNPs@CH-POMs (*via* charge-mediated adsorption), thereby enhancing the utilization of the UV light emitted by the UCNPs, and further improving the system's targeted therapeutic efficacy. The UCNPs(Tm/Er)@CH-POM nanoplatform integrates NIR responsiveness, tunable luminescence, and targeted drug delivery, making it a promising candidate for both generalized anionic drug delivery and specific AD photodynamic therapy. This work not only provides a versatile nanocarrier design but also offers new insights into the application of upconversion materials in photooxidative treatment of neurodegenerative diseases such as AD.

Author contributions

Xiaofeng Jia: methodology, formal analysis, data curation, and writing – original draft; Yijia Guan: conceptualization, supervision, writing – review & editing, visualization, and funding acquisition; Weijie Cao: methodology, formal analysis, investigation, data curation, and visualization; Xiaoshuo Zhang: methodology, validation, investigation, and visualization; Huazhen Duan: validation and funding acquisition; Hui Guo: methodology, validation, and investigation; Huichang Chen: validation; Binbin Wang: resources; Tao Li: methodology, writing – review & editing, supervision, project administration, and funding acquisition; Jianguo Liao: resources and supervision.

Conflicts of interest

The authors declare no competing financial interest.

Data availability

The authors confirm that the data supporting the findings of this study are available within the article and its supplementary information (SI). Supplementary information: particle width distribution curve, particle length distribution, EDS elemental analysis, content of elements, XPS spectra, FTIR spectra, UV-Vis absorption spectra and fluorescence spectra of DCF. See DOI: https://doi.org/10.1039/d5dt03121d.

Acknowledgements

This research was funded by the National Natural Science Foundation of China (21907024 and 21905078), Natural Science Foundation of Henan Province (252300421448 and 242300420189), the Fundamental Research Funds for the Universities of Henan Province (NSFRF230407 and NSFRF240808), Funding Plan for Young Backbone Teachers of Henan Polytechnic University (2024XQG-04), Doctoral Foundation of Henan Polytechnic University (B2018-47 and B2019-37), and Henan Provincial Innovation and Entrepreneurship Training Program for Undergraduates (S202510460065).

References

1 J. Gaugler, B. James, T. Johnson, J. Reimer, M. Solis, J. Weuve, R. F. Buckley and T. J. Hohman, Alzheimer's disease facts and figures, *Alzheimer's Dementia*, 2022, **18**, 700–789.
2 P. Scheltens, B. D. Strooper, M. Kivipelto, H. Holstege, G. Chetelat, C. E. Teunissen, J. Cummings and W. M. van der Flier, Alzheimer's disease, *Lancet*, 2021, **397**, 1577–1590.
3 D. S. Knopman, H. Amieva, R. C. Petersen, G. Chetelat, D. M. Holtzman, B. T. Hyman, R. A. Nixon and D. T. Jones, Alzheimer disease, *Nat. Rev. Dis. Primers*, 2021, **7**, 33.
4 M. Tolar, S. Abushakra and M. Sabbagh, The path forward in Alzheimer's disease therapeutics: Reevaluating the

amyloid cascade hypothesis, *Alzheimer's Dementia*, 2020, **16**, 1553–1560.
5 C. E. Conti Filho, L. B. Loss, C. Marcolongo-Pereira, J. V. Rossoni Junior, R. M. Barcelos, O. Chiarelli-Neto, B. S. D. de Silva, R. Passamani Ambrosio, F. C. A. Q. Castro, S. F. Teixeira and N. J. Mezzomo, Advances in Alzheimer's disease's pharmacological treatment, *Front. Pharmacol.*, 2023, **14**, 1101452.
6 A. Gustavsson, N. Norton, T. Fast, L. Froelich, J. Georges, D. Holzapfel, T. Kirabali, P. Krolak-Salmon, P. M. Rossini, M. T. Ferretti, L. Lanman, A. S. Chadha and W. M. van der Flier, Global estimates on the number of persons across the Alzheimer's disease continuum, *Alzheimer's Dementia*, 2023, **19**, 658–670.
7 S. Srivastava, R. Ahmad and S. K. Khare, Alzheimer's disease and its treatment by different approaches: A review, *Eur. J. Med. Chem.*, 2021, **216**, 113320.
8 E. Karran and B. D. Strooper, The amyloid hypothesis in Alzheimer disease: new insights from new therapeutics, *Nat. Rev. Drug Discovery*, 2022, **21**, 306–318.
9 Y. Guan, W. Cao, T. Li, J. Qin, Q. He, X. Jia, Y. Li, Y. Zhang and J. Liao, NIR-excited upconversion nanoparticles used for targeted inhibition of Aβ42 monomers and disassembly of Aβ42 fibrils, *J. Mater. Chem. B*, 2023, **11**, 1445–1455.
10 W. Chen, J. Li, J. Guo, L. Li and H. Wu, Diagnosis and therapy of Alzheimer's disease: Light-driven heterogeneous redox processes, *Adv. Colloid Interface Sci.*, 2024, **332**, 103253.
11 B. I. Lee, Y. J. Chung and C. B. Park, Photosensitizing materials and platforms for light-triggered modulation of Alzheimer's β-amyloid self-assembly, *Biomaterials*, 2019, **190–191**, 121–132.
12 W. Liu, X. Dong, Y. Liu and Y. Sun, Photoresponsive materials for intensified modulation of Alzheimer's amyloid-β protein aggregation: A review, *Acta Biomater.*, 2021, **123**, 93–109.
13 P. Bondia, J. Torra, C. M. Tone, T. Sawazaki, A. del Valle, B. Sot, S. Nonell, M. Kanai, Y. Sohma and C. Flors, Nanoscale View of Amyloid Photodynamic Damage, *J. Am. Chem. Soc.*, 2020, **142**, 922–930.
14 Z. Ye, L. Li, Q. Duan, X. Sheng, C. Zhang, X. Fan, Z. Li and L. Xiao, KLVFF-Guided Molecular Scissors: a Trojan Horse Strategy for Precision Photodynamic Dissolution of Aβ Aggregates, *Adv. Healthcare Mater.*, 2025, **14**, 2502595.
15 T. Hou, Q. Yang, M. Ding, X. Wang, K. Mei, P. Guan, C. Wang and X. Hu, Blood-brain barrier permeable carbon nano-assemblies for amyloid-beta clearance and neurotoxic attenuation, *Colloids Surf., B*, 2024, **244**, 114182.
16 K. Kang and S. Bacci, Photodynamic Therapy, *Biomedicines*, 2022, **10**, 2701.
17 G. M. Cramer, K. A. Cengel and T. M. Busch, Forging Forward in Photodynamic Therapy, *Cancer Res.*, 2022, **82**, 534–536.
18 Z. Ye, L. Li, Q. Duan, X. Sheng, C. Zhang, X. Fan, Z. Li and L. Xiao, KLVFF-Guided Molecular Scissors: a Trojan Horse Strategy for Precision Photodynamic Dissolution of Abeta Aggregates, *Adv. Healthcare Mater.*, 2025, **14**, e2502595.
19 Y. Heo, K. Kim, J. Kim, J. Jang and C. B. Park, Near-Infrared-Active Copper Bismuth Oxide Electrodes for Targeted Dissociation of Alzheimer's β-Amyloid Aggregates, *ACS Appl. Mater. Interfaces*, 2020, **12**, 23667–23676.
20 J. Yang, X. Wang, J. Liu, W. Chi, L. Zhang, L. Xiao and J.-W. Yan, Near-Infrared Photooxygenation Theranostics Used for the Specific Mapping and Modulating of Amyloid-β Aggregation, *Anal. Chem.*, 2022, **94**(45), 15902–15907.
21 F. He, L. Feng, P. Yang, B. Liu, S. Gai, G. Yang, Y. Dai and J. Lin, Enhanced up/down-conversion luminescence and heat: Simultaneously achieving in one single core-shell structure for multimodal imaging guided therapy, *Biomaterials*, 2016, **105**, 77–88.
22 N. Jurga, M. Runowski and T. Grzyb, Lanthanide-based nanothermometers for bioapplications: excitation and temperature sensing in optical transparency windows, *J. Mater. Chem. C*, 2024, **12**, 12218–12248.
23 Y. Y. Liu, X. F. Meng and W. B. Bu, Upconversion-based photodynamic cancer therapy, *Coord. Chem. Rev.*, 2019, **379**, 82–98.
24 K. Du, J. Feng, X. Gao and H. Zhang, Nanocomposites based on lanthanide-doped upconversion nanoparticles: diverse designs and applications, *Light:Sci. Appl.*, 2022, **11**, 222.
25 W. Zheng, P. Huang, D. Tu, E. Ma, H. Zhu and X. Chen, Lanthanide-doped upconversion nano-bioprobes: electronic structures, optical properties, and biodetection, *Chem. Soc. Rev.*, 2015, **44**, 1379–1415.
26 B. Saha, A. Ghosh, A. Singh and S. K. Sahu, Amplification of luminescence intensity by ytterbium(III) dopant in upconversion nanoparticles integrated with carbon dots for NIR-responsive targeted photodynamic therapy, *Dalton Trans.*, 2025, **54**, 13071.
27 X. Zhu, J. Zhang, J. Liu and Y. Zhang, Recent Progress of Rare-Earth Doped Upconversion Nanoparticles: Synthesis, Optimization, and Applications, *Adv. Sci.*, 2019, **6**, 1901358.
28 S. Zhang, S. Qin, Y. Xiao, Z. Liu, X. Hu, Z. Xiao, D. Huang, L. Han and X. Ye, Near-infrared luminescent materials: a review of their practical applications and prospective advancement, *Dalton Trans.*, 2025, **54**, 6717.
29 Y. Fan, L. Liu and F. Zhang, Exploiting lanthanide-doped upconversion nanoparticles with core/shell structures, *Nano Today*, 2019, **25**, 68–84.
30 A. A. Ansari, A. K. Parchur, Y. Li, T. Jia, R. Lv, Y. Wang and G. Chen, Cytotoxicity and genotoxicity evaluation of chemically synthesized and functionalized upconversion nanoparticles, *Coord. Chem. Rev.*, 2024, **504**, 215672.
31 Z. Luo, D. Mao, X. Li, J. Luo, C. Gong and X. Liu, Lanthanide-based nanoparticles for cancer phototherapy, *Coord. Chem. Rev.*, 2024, **508**, 215773.
32 A. Sedlmeier and H. H. Gorris, Surface modification and characterization of photon-upconverting nanoparticles for bioanalytical applications, *Chem. Soc. Rev.*, 2015, **44**, 1526–1560.
33 P. Kowalik, I. Kamińska, K. Fronc, A. Borodziuk, M. Duda, T. Wojciechowski, K. Sobczak, D. Kalinowska, M. T. Klepka and B. Sikora, The ROS-generating photosensitizer-free $NaYF_4$:

Yb,Tm@SiO_2 upconverting nanoparticles for photodynamic therapy application, *Nanotechnology*, 2021, **32**, 475101.

34 T. Ueda, M. Suzuki and T. Toya, The Enhancement of the formation of Wells–Dawson-type polyoxometalates by the addition of high concentrations of LiCl, *J. Cluster Sci.*, 2016, **27**, 501–511.

35 P. Chakraborty, M. Link, C. Plett, M. Neumaier, P. Weis, M. Ibrahim, S. Grimme and M. M. Kappes, Polyoxometalate-cyclodextrin aggregates in isolation: probing the conformer space and binding affinities, *Nanoscale*, 2025, **17**, 22988.

36 M. Moghadasi, M. Abbasi, M. Mousavi and M. Mirzaei, Polyoxometalate-based materials in therapeutic and biomedical applications: current status and perspective, *Dalton Trans.*, 2025, **54**, 6333.

37 X. H. Zhang, D. C. Tang, L. He and Y. W. Cao, Polyoxome talates Based Catalysts for Carbonylation Reactions: A Review, *Chem. – Asian J.*, 2024, **19**, e202400464.

38 X. T. Xu, Y. F. Guo, B. L. Li, Y. F. Lv, Z. H. Wu, S. Y. Liang, L. He and Y. F. Song, Polyoxometalates emerging as multifunctional powerhouses in the battle against cancer, *Coord. Chem. Rev.*, 2025, **522**, 216210.

39 M. Ma, Z. Liu, H. Zhao, H. Zhang, J. Ren and X. Qu, Polyoxometalates: metallodrug agents for combating amyloid aggregation, *Natl. Sci. Rev.*, 2024, **11**, nwae226.

40 N. Gao, Z. Liu, H. Zhang, C. Liu, D. Yu, J. Ren and X. Qu, Site–Directed Chemical Modification of Amyloid by Polyoxometalates for Inhibition of Protein Misfolding and Aggregation, *Angew. Chem., Int. Ed.*, 2022, **61**, e202115336.

41 N. Gao, H. Sun, K. Dong, J. Ren, T. Duan, C. Xu and X. Qu, Transition-metal-substituted polyoxometalate derivatives as functional anti-amyloid agents for Alzheimer's disease, *Nat. Commun.*, 2014, **5**, 3422.

42 J. Chen, W. Z. Yang, H. Chen, X. Ding, H. Chen, C.-H. Zhan and Z. Jin, Targeting protein aggregation: the promising application of polyoxometalates in neurodegenerative diseases, *Inorg. Chem. Front.*, 2024, **11**, 7238–7255.

43 M. Perxés Perich, S. Palma-Florez, C. Sole, S. Gobernado-Ferron, J. Samitier, P. Gomez-Romero, M. Mir and A. Lagunas, Polyoxometalate-Decorated Gold Nanoparticles Inhibit beta-Amyloid Aggregation and Cross the Blood-Brain Barrier in a physiological Model, *Nanomaterials*, 2023, **13**, 2697.

44 M. Li, C. Xu, J. Ren, E. Wang and X. Qu, Photodegradation of β-sheet amyloid fibrils associated with Alzheimer's disease by using polyoxometalates as photocatalysts, *Chem. Commun.*, 2013, **49**, 11394–11396.

45 M. H. Karami, M. Pourmadadi, M. Abdouss, M. R. Kalaee, O. Moradi, A. Rahdar and A. M. Diez-Pascual, Novel chitosan/gamma-alumina/carbon quantum dot hydrogel nanocarrier for targeted drug delivery, *Int. J. Biol. Macromol.*, 2023, **251**, 126280.

46 J. Liu, L. Zhang, H. Ma, H. Sun, S. A. Ge, J. Liu, S. Fan and C. Quan, Quaternary ammonium chitosan-functionalized mesoporous silica nanoparticles: A promising targeted drug delivery system for the treatment of intracellular MRSA infection, *Carbohydr. Polym.*, 2025, **352**, 123184.

47 P. Yadav, S. G. Warkar and A. Kumar, Fabrication of carboxymethyl tamarind kernel gum-based pH-responsive hydrogel composite for oral delivery of azithromycin drug, *Int. J. Biol. Macromol.*, 2025, **322**(Pt 2), 146662.

48 Y. Guan, H. Guo, X. Jia, J. Qin, Y. Yang, K. Cao, T. Li, J. Liao and Y. Zhang, Regulation of Glass Transition Temperature in Thermo–Responsive Epoxy Shape Memory Polymers: The Roles of Chemical Crosslinking Density and Chain Flexibility, *J. Polym. Sci.*, 2024, **63**, 406–416.

49 I. M. Mbomekalle, Y. W. Lu, B. Keita and L. Nadjo, Simple, high yield and reagent-saving synthesis of pure α-$K_6P_2W_{18}O_{62}\cdot 14H_2O$, *Inorg. Chem. Commun.*, 2004, **7**, 86–90.

50 Y. Guan, D. Yu, H. Sun, J. Ren and X. Qu, Aβ aggregation behavior at interfaces with switchable wettability: a bioinspired perspective to understand amyloid formation, *Chem. Commun.*, 2021, **57**, 2641–2644.

